Ultra-high-speed hybrid ceramic triboelectric bearing with real-time dynamic instability monitoring

Shuai Gao [a,b], Qinkai Han [a,*], Xuening Zhang [c], Paolo Pennacchi [b], Fulei Chu [a]

[a] State Key Laboratory of Tribology, Department of Mechanical Engineering, Tsinghua University, Beijing 100084, China
[b] Department of Mechanical Engineering, Politecnico di Milano, Via G. La Masa 1, 20156 Milan, Italy
[c] Aero Engine Academy of China, Beijing 101304, China

ABSTRACT

The reliability and stability of bearing operation are crucial factors limiting the performance of high-speed rotating machinery. In this study, an ultra-high-speed hybrid ceramic rolling element triboelectric bearing (US-HCTEB) was developed to provide real-time dynamic behavior and stability monitoring. Herein, we adopted a floating rolling–sliding combination freestanding mode that ensures bearing structural integrity. Furthermore, a crown-shaped cage was employed with an opening, allowing the ceramic rolling element to be used as a dielectric material that was coupled with a sector-shaped interdigital electrode set on the bearing end cover to form a floating freestanding triboelectric nanogenerator (TENG). The rolling element self-rotated and revolved owing to the traction of the raceways, sweeping the electrodes to generate an alternating current. Additionally, the superiority and reliability of the US-HCTEB were demonstrated using a 30 million cycle durability test and an ultra-high rotating speed test at 16000 rpm, which far exceeds the capabilities of previously reported triboelectric bearings. The US-HCTEB output was then evaluated considering variable working conditions, structural optimization, and the surrounding environment. Dry contact lubrication and low humidity were found to be beneficial for the output performance. The spectra of the output current and the statistics describing the rolling element instantaneous speed suggest that the high-speed heavy radial load of the US-HCTEB could reduce overall skidding at the cost of increased instability. Subsequently, an extremely fast acceleration and deceleration test program was conducted on the US-HCTEB to evaluate its performance under the complex and nonstationary conditions in which high-speed bearings operate. The results revealed that the US-HCTEB not only achieved real-time and high-resolution dynamic behavior identification but also exhibited high reliability as it functioned appropriately until bearing failure. Thus, the proposed high-precision US-HCTEB can serve as an essential basis for the development of smart rolling bearings.

1. Introduction

With the rapid development of high-speed machine tools, aerospace engines, and similar equipment, the requirements for the dynamic performance, service life, and stability of key component rolling bearings operating at high speeds have become increasingly stringent [1–4]. Generally, a bearing with a DN value (defined as the product of the bearing inner diameter [mm] and the rotation speed [rpm]) greater than 0.6×10^6 mm·rpm is considered to be a high-speed bearing. Dynamic instabilities such as rolling element skidding [5,6], cage wear [7–9], unstable cage whirling, and even twisted fracture [4,10] represent the root cause of failure and reliability reduction of high-speed roller

bearings. Traditional methods for monitoring bearing dynamics (skidding, cage stability, etc.), such as tacho sensors [11–13], fiber optic sensors [14], and high-speed photographical methods [15], are limited by structural integrity, real-time performance, and measuring precision issues, and they are difficult to apply in compact spaces and under ultra-fast acceleration conditions. Therefore, it is critical that advanced technologies be applied to develop high-precision, compact intelligent bearing systems to monitor bearing health status in real-time.

A triboelectric nanogenerator (TENG) [16–23] is an advanced technology based on the coupling effect of contact electrification and electrostatic induction and has received overwhelming attention owing to its excellent capabilities in the fields of mechanical energy harvesting

[24–26], self-powering sensing [27–29], and environmental monitoring [30]. Furthermore, its light weight, structural flexibility, and environmental friendliness correspond to the objectives of intelligence and carbon neutralization in modern industry [20,31,32]. Recently, TENG-inspired intelligent rolling bearings have been developed that can significantly improve the condition monitoring level of rotating equipment [33]. Meng et al. [34] proposed a TENG-inspired rolling bearing sensor to monitor the bearing motion state for the first time by adopting a rolling freestanding mode. Several scholars [28,29,36] have extended the application of triboelectric bearings to enhance the output performance of cylindrical and tapered roller bearings. Han et al. [27,37] and Xie et al. [38,39] addressed the possibility of premature wear failure caused by direct contact [40,41] between rolling elements and electrodes in such triboelectric bearing structures. Furthermore, several non-contact intelligent bearings, suitable for non-metallic and metallic bearings, that provide real-time monitoring of bearing cage stability and skidding have been proposed [6,39]. Although these schemes can ensure the structural integrity of the bearing, the accompanying modifications to the triboelectric structure will more or less interfere with the dynamic behavior of the rolling element or the cage itself [6,27,39], thus disturbing the running stability of the bearing. Alternatively, the dynamic behavior of the bearing can be monitored indirectly through the motion of the cage rather than that of the rolling element. However, this affects real-time monitoring performance under extremely fast acceleration and deceleration conditions. Indeed, the rotational speed limits of most previously reported triboelectric bearing prototypes, including SLB-TENG [41], TRSS [38], B-TENG [42], RTB [27], TRBB [37], SRB [35], SPRS [34], NC-TEBS [39], and HP-TEBSS [6], are all less than 5000 rpm, their DN values are all less than 0.15×10^6 mm·rpm, and their effectiveness under extremely fast acceleration conditions has not been validated. As a result, it is difficult to apply these bearing designs to realize bearing health monitoring in high-speed and ultra-high-speed scenarios, significantly limiting the potential applications of intelligent triboelectric bearings.

To address this limitation, a high-precision crown-shaped cage (developed by SKF Co. for high-speed scenarios up to a DN value of 1.8×10^6 mm·rpm) was used in this study to develop an ultra-high-speed hybrid ceramic rolling element triboelectric bearing (US-HCTEB) that realizes real-time monitoring of bearing dynamic instability. The innovative features of the research lie in: firstly, A floating, non-contact, rolling–sliding combination freestanding mode is adopted in this bearing, and its original structural integrity and running status is completely unaffected by the addition of the TENG. Secondly, The US-HCTEB is capable of working stably at speeds up to 16000 rpm, which is considered an ultra-high-speed scenario, unlike other TENG-based bearings. Finally, a new method for evaluating bearing stability based on a large amount of transient bearing skidding data monitored by US-HCTEB, and its dynamic instability behavior was systematically investigated. The floating non-contact rolling–sliding freestanding layer is realized using a self-rotating and revolving ceramic rolling element, and an interdigital electrode stator plate is attached to the end cover mounted on the side surface of the bearing outer ring corresponding to the opening direction of the crown-shaped cage. Thus, as the bearing rotates, the inner ring drives the rolling element to self-rotate and revolve around the bearing axis, generating spinning and sliding relative to the fixed metal interdigital electrodes. The resulting electrostatic induction generates sinusoidal electrical signals, the instantaneous frequencies of which can indicate the skidding and stability states of the bearing.

The effects of the rolling element material, number of electrode pairs, environmental humidity, bearing temperature, and bearing lubrication state on the performance and skidding of the proposed US-HCTEB were investigated in this study. Additionally, durability tests and friction torque analyses were performed to demonstrate the advanced performance of the US-HCTEB. Finally, an application scenario involving extremely fast acceleration and deceleration was implemented using the US-HCTEB to demonstrate its superiority and accuracy in real-time dynamic behavior monitoring. An unexpected cage failure caused by repeated extreme acceleration tests indicated that the integrated TENG was more reliable than the bearing itself.

2. Results and discussion

2.1. Structure and working mechanism of US-HCTEB

Ribbon cages and integral cages made of metal are commonly used in traditional low-speed rolling bearings; a crown-shaped cage has been developed by a high-tech bearing company for ultra-high-speed applications, such as high-speed motors due to its excellent toughness performance, wear resistance and corrosion resistance. The design principle of the crown-shaped cage rests upon the removal of parts that do not contribute to the strength and stiffness of the cage to reduce its weight as much as possible. The optimum cage shape under high-speed bearing rotation can be deduced using the topology optimization method. The cage stability may be affected by the eccentricity between cage mass center and the central surface of the pocket. Thus, a real-time monitoring on bearing running stability is important and indispensable. For bearings with ceramic balls, as the clearance is constant, the bearing can be allowed to work in an environment with severe temperature changes, which provides a guarantee for the bearing to operate at high speed and high temperature.

This crown-shaped cage is made of a high-stiffness resin material; the prototype employed in this study was made of polyetheretherketone (PEEK), which is reported to be more effective than traditional metal in restraining the deformation of the cage under high-speed rotation. As can be seen in the exploded and assembled views in Fig. 1(a) and (b), respectively, the proposed US-HCTEB utilizes the space at the opening of the crown-shaped cage and comprises a dielectric ceramic rolling element rotator and copper electrode stator. Interdigital electrodes with nine pairs of comb fingers are laid on the epoxy plate using the copper cladding process, and the printed circuit board (PCB) is adhered to the acrylic end cover using a strong glue. The shoulder of the acrylic end cover forms an interference fit with the inner shoulder of the bearing outer ring, and a set of strong neodymium-boron magnets is embedded on the acrylic end cover to fix the position of the TENG relative to the outer ring of the bearing. Fig. 1(c) shows the matching of the TENG assemblies with the crown-shaped cage hybrid bearing to fabricate the prototype US-HCTEB. The average diameter of the interdigital electrodes should correspond to the bearing pitch diameter to ensure the maximum output of the US-HCTEB in the floating-ball spinning–sliding mode. The detailed structure and fabrication process of the proposed US-HCTEB are shown in Fig. S1 and S2 (Supporting Information), respectively. During the design process, sufficient clearance was ensured between the outer shoulder of the inner ring of the bearing and the inner ring of the end cover to avoid rubbing. Furthermore, the clearance between the rotator and stator was confirmed to be larger than the maximum possible axial movement of the rolling elements to avoid wear on the electrodes and interference with the motion of the rolling elements. It means that the US-HCTEB does not need to modify the original structure of the bearing itself, which ensures the structural integrity. And the clearance ensures that the structure of the TENG does not limit the high speed capability of the bearing itself. However, this advantage is traded by sacrificing the current output intensity of TENG.

Three US-HCTEBs and a companion bearing were installed on the main shaft of an ultra-high-speed bearing test platform driven by a high-speed motorized spindle, as shown in Fig. 1(d). The four bearings were located in three loading chambers, of which the first chamber was subjected to horizontal radial forces in opposite directions and the second and third chambers were subjected to radial forces in the same direction. Thermocouple probes were placed on the outer surface of each bearing. The detailed test platform control and signal acquisition
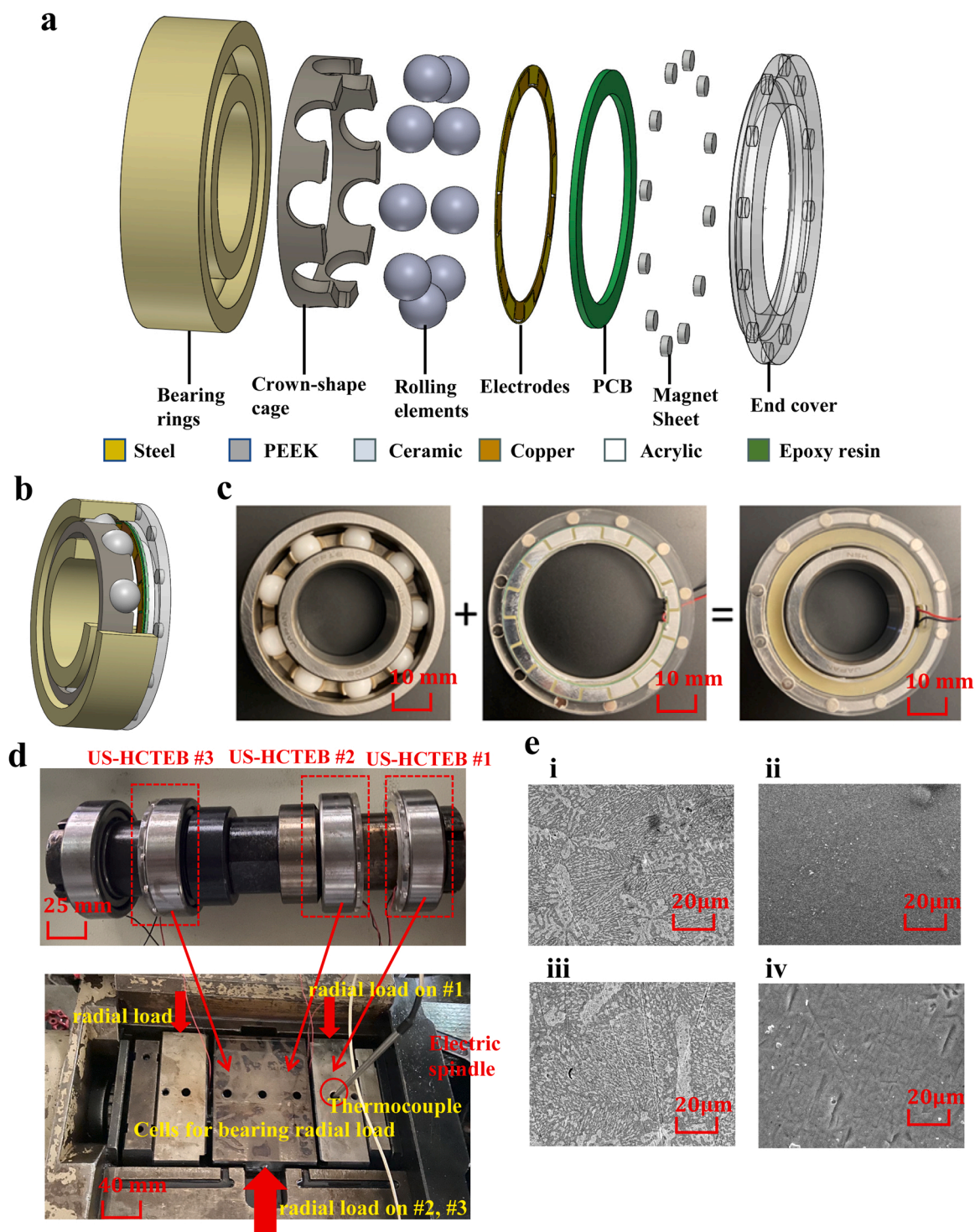
Fig. 1. Structural design and test platform of the US-HCTEB based on the crown-shape-cage and floating spinning-sliding freestanding mode TENG: (a) the exploded view of the US-HCTEB, (b) the assembled view of the US-HCTEB, (c) the prototype of the US-HCTEB, (d) the arrangement of the tested US-HCTEBs and the over-view of the test platform, (e) the magnified scanning electron microscope (SEM) photo of the electrodes and rolling elements (i, ii: before test; iii, iv: after long-term operation).

systems are presented in Fig. S3 and S4 (Supporting Information), respectively. Fig. 1(e) shows the scanning electron microscopy (SEM) images of the electrode and a ceramic rolling element of the US-HCTEB before and after testing. Owing to long-term wear and slight skidding, slight spalling and pitting can be observed to have occurred on the surface of the rolling element. The surface morphologies of the electrodes remained essentially the same before and after testing.

As the inner ring of the bearing rotates, the rolling elements are driven to self-rotate and revolve around the bearing axis by the frictional force along the inner raceway contact area. The floating freestanding dielectric rolling elements thus sweep along the interdigital electrodes in a spinning and sliding manner, generating alternating current (AC). The rolling element instantaneous revolution frequency is equal to the AC frequency divided by the number of electrode pairs (N_e). Diagrams of the

motion state and working mechanism of the US-HCTEB components are presented in Fig. 2(a) and (b), respectively. Although the floating-ball spinning and sliding sweeps occur simultaneously, the electrons transferred repeatedly between electrodes A and B are mainly driven by the electrostatic force of the circumferential sliding–sweeping ball motion. The AC for each working cycle can be divided into four phases. In phase 1, the crown-shaped cage exposes a part of the rolling element surface such that it faces the surface of electrode A. Subsequently, similar quantities of charge accumulate on the surfaces of the ball and electrode, reaching electrostatic equilibrium, as shown in Fig. 2 (b1). In phase 2, as the rolling element is driven to leave electrode A, the negative charges on its surface attract the positive charges to electrode B, and an instantaneous current occurs between the electrodes, as shown in Fig. 2 (b2). In phase 3, the rolling element faces electrode B, causing another electrostatic equilibrium to develop and no current to be present in this transient moment, as shown in Fig. 2 (b3). Finally, in phase 4, the continuous ball revolution induces a phenomenon similar to that in phase 2, but with the current in the opposite direction, as shown in Fig. 2 (b4).

The potential distribution between the rotator and the electrodes was calculated in this study using the COMSOL finite element software, as shown in Fig. 2(c). The simulated moment was found to correspond to the running state of the bearing, as shown in Fig. 2(a); the maximum potential occurred at positions 1 and 3. The qualitative analysis thus validated the working mechanism of AC generation, as shown in Fig. 2 (b).

2.2. Optimization of the US-HCTEB

Each US-HCTEB prototype tested on the high-speed bearing test platform was fabricated using a 6206 deep-groove ball bearing. The critical structural parameters include the number of balls (equal to the number of electrode fingers, $N_b = N_e = 9$), ball diameter ($D = 9.56$ mm), and bearing pitch diameter ($d_m = 46.64$ mm). A high-speed electric spindle with a rotating speed range (3000–30000 rpm) controlled by a frequency converter and a counterweight-balanced hydraulic loading system were employed to characterize the US-HCTEB. The variations in the output waveform of the short-circuit current I_s, open-circuit voltage V_o, and transferred charge Q are presented in Fig. 3(a) and (b) as the bearing rotation speed ω_i varies from 3000 to 15,000 rpm and the bearing radial load F_r varies from 0 to 600 N, respectively. All signal waveforms were acquired under constant operating conditions. In terms of the lateral comparison in Fig. 3 (a1–3) and (b1–3), the trends of I_s, V_o, and Q show similar characteristics with increasing ω_i and F_r. This is significantly different from other triboelectric bearings fabricated using cages [6,27,39] because the US-HCTEB was established based on the revolution and spinning of the rolling elements. Indeed, the movements and positions of the rolling elements are more sensitive to variations in speed and load than those of the cage.

Considering the change in Q shown in Fig. 3 (a3) as an example, the amplitude of Q first increases then decreases before increasing again as ω_i increases continuously, reaching an initial maximum value of 0.17 nC at 6000 rpm and a local minimum of 0.12 nC at 8000 rpm. It is calculated that the first order critical speed of the simplified rotor is approximately 8500 rpm. And it can be assumed that the reason for this unusual decreasing trend is that the rotor vibration was intensified as
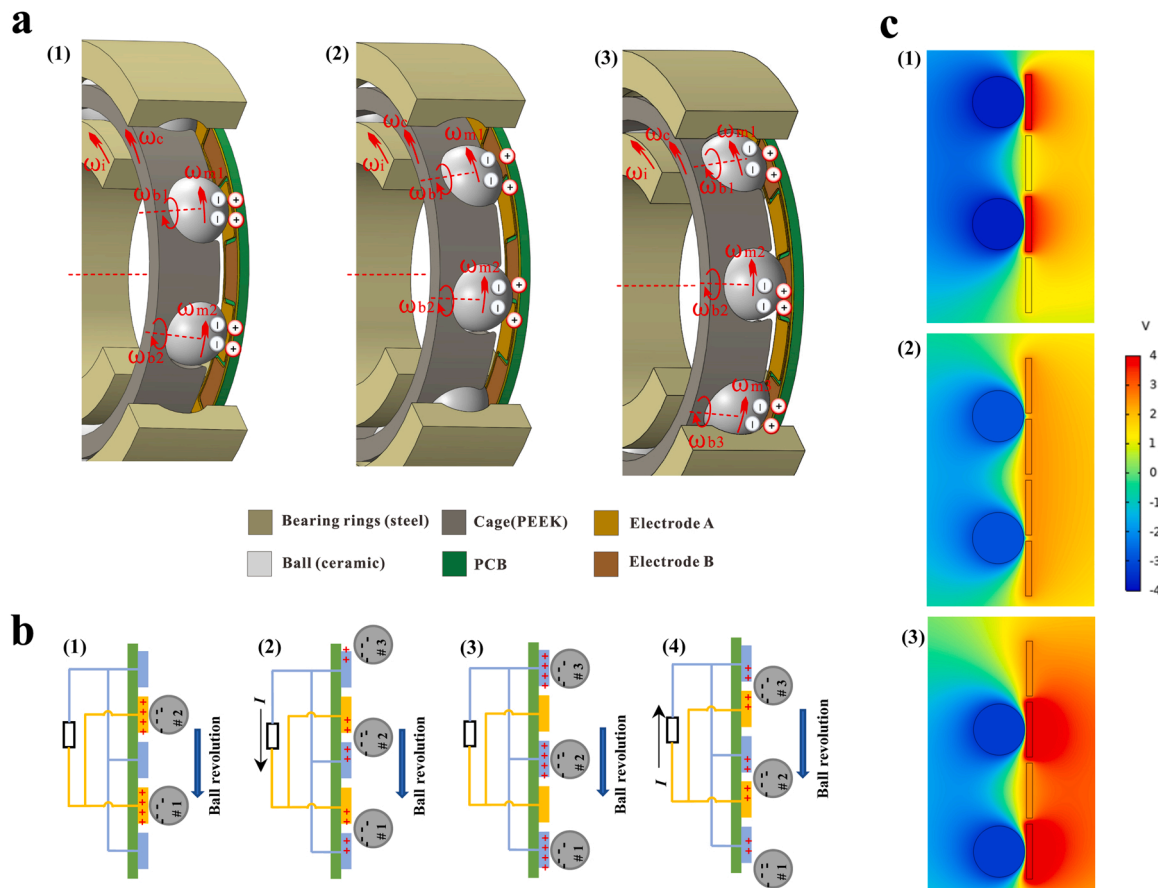

Fig. 2. Schematic diagram of working principle of US-HCTEB with floating spinning-sliding freestanding mode: (a) the motion state of the components of the US-HCTEB, (b) current and charge distribution of a full working cycle in driving an external load, (c) calculated potential distributions by COMSOL corresponds to the position of (a).
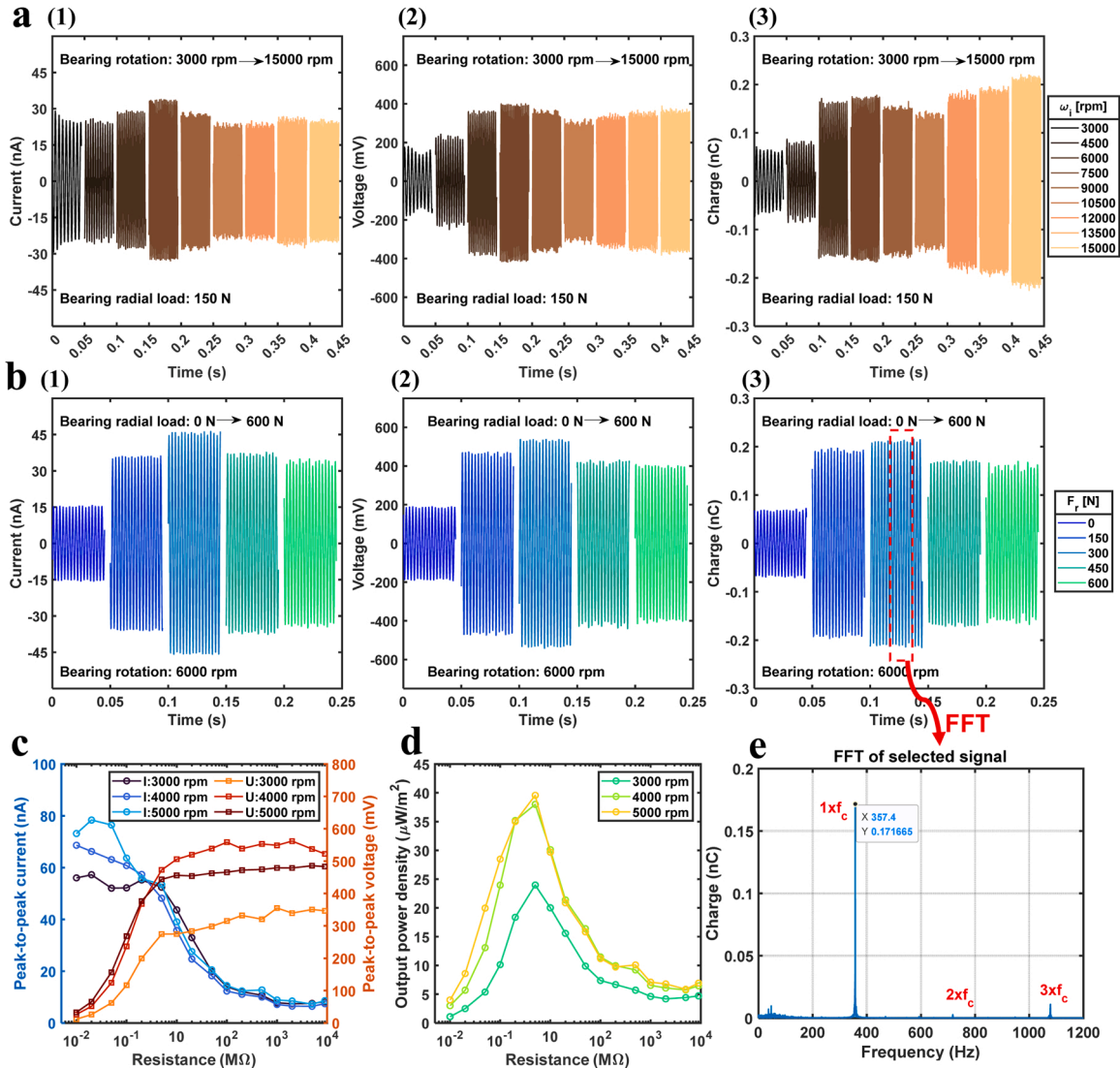
Fig. 3. Output performance of the US-HCTEB: (a) I_s, V_o, Q_c under various bearing rotating speed, (b) I_s, V_o, Q_c under various bearing radial load, (c) output voltage and current under various external load of three kinds of rotating speed, (d) output power of the US-HCTEB, (e) the FFT spectrum for indicating the rolling elements revolution speed.

the rotation speed located in the critical speed region, which is the 7000–9000 rpm range. It could affect the running stability of the rolling elements and resulting in weakened electrostatic induction. In addition to the absence of performance improvement realized by using the rolling elements as the dielectric element instead of the cage, previously reported triboelectric bearings [6,27,39] were not subjected to such high ω_i, explaining why this phenomenon has not been previously observed.

The axial preload was applied to eliminate bearing clearance using the test platform structure and loading scheme depicted in Fig. 1(d). When F_r was first applied, the inner ring and rolling elements deflected slightly [2], changing the axial clearance c_a between the rolling elements and the electrode and thereby directly affecting the output of the US-HCTEB [6]; the continued increase in F_r caused a bending moment in the shaft. These factors combined to produce the US-HCTEB output trends shown in Fig. 3(b), which shows that with an increase in F_r, the values of I_s, V_o, and Q initially increase before decreasing to steady states, reaching maxima at approximately $F_r = 300$ N. Theoretically, Q and output current I can be quantitatively determined based on the floating freestanding TENG mechanism as follows:

$$Q = \int_0^{\frac{\pi}{N_b}} \sigma_c d_m (R_o - R_i) d\theta, \tag{1}$$

$$I = \frac{dQ}{dt}, \tag{2}$$

where σ_c is the surface charge density; R_o and R_i are the outer and inner radius of the electrode area, respectively; and θ is the angular position of the bearing.

The peak output current, voltage, and power density obtained as the US-HCTEB drove the external load under three ω_i values are demonstrated in Fig. 3(c) and (d). As the resistance varies from 10 kΩ to 9 GΩ, the peak voltage increases to 600 mV and the current decreases to 7 nA; the maximum output power density can be observed when the external resistance is approximately equal to 5 MΩ. The value of ω_i had no significant effect on the optimum resistance. Fig. 3(e) shows the featured frequency of the selected signal. According to the working mechanism of the floating freestanding US-HCTEB and the featured frequency of the bearing in a pure rolling state, the theoretical and measured rolling element revolution frequencies f_{bm} and f_{br} can be describedby the following equations:

$$f_{bm} = \frac{1}{120} \omega_i \left(1 - \frac{D}{d_m} \cos\alpha_0 \right), \tag{3}$$

$$f_c = N_e f_{br}, \tag{4}$$

where f_c, is the featured frequency of the signal, α_0 is the nominal bearing contact angle. Due to the axial preload is applied on the test rig, it is calculated the bearing contact angle is 20°. The featured order of cage can be calculated to be 0.404. Based on the working conditions shown in Fig. 3(e), f_{bm} = 40.4 Hz and f_{br} = 39.71 Hz. The overall rolling element skidding degree can then be obtained as b_{sk} = $100\% * (f_{bm} - f_{br})/f_{bm}$ = 1.7%.

The following discussion explores the optimization of the US-HCTEB structural parameters based on its output performance and skidding according to the applied design parameters and the influence of the surrounding environmental parameters. Due to the output stability of current signal under variable speed and its equivalence with voltage signal for condition monitoring of bearing running state, the amplitude and waveform of I_s were chosen as indicators. And the analysis for indicator selection is presented in Fig. S5 and S6 (Supporting Information). First, three types of rolling elements constructed using different dielectric ceramic materials—zirconia (ZrO_2), silicon nitride (SiN_4), and silicon carbide (SiC)—were evaluated. Photographs of the three bearing types are shown in Fig. S7 (Supporting Information). The peak-to-peak amplitudes of I_s under different ω_i and F_r values are presented in Fig. 4(a) and (b), respectively, in which the ranking of I_s values according to the bearing material is SiC < SiN_4 < ZrO_2. The sudden decrease of I_s for test case F_r = 600N is caused by the instability of rotor as it is located in the critical speed range. The difference according to bearing material is particularly noticeable under heavy-load conditions. Therefore, the entire series of experiments in this study was performed using rolling elements made of ZrO_2.

Subsequently, the effects of the electrode area and number of electrode fingers on the output current and monitoring accuracy of the US-HCTEB were explored. A group of electrodes with an electrode width E_w = 4 mm and N_e values of 9 and 18 were compared with another group of electrodes with N_e = 9 and E_w values of 4 and 8 mm. The detailed configurations and dimensions of these three-electrode plates are shown in Fig. S8 (Supporting Information). The peak-to-peak amplitudes of I_s under different ω_i values are presented in Fig. 4(c). The ranking of I_s according to electrode parameters is $[N_e = 18, E_w = 4mm]\langle[N_e = 9, E_w = 8mm]\langle[N_e = 9, E_w = 4mm]$, with the amplitude of I_s for $[N_e = 9, E_w = 8mm]$ fluctuating significantly with increasing ω_i. Fig. 4(d) presents the precision of the measured instantaneous revolution speed [6] of the rolling elements tested using the three types of electrodes within 0.05 s. It can be observed that the information regarding the instantaneous speed obtained by the N_e = 18 electrode is twice that obtained by the N_e = 9 electrode, indicating that 18 electrodes can more accurately describe the dynamic bearing behavior. However, an increase in N_e is not conducive to improving the output characteristics of the US-HCTEB, and the area of the electrode is not positively correlated with the amplitude of I_s. Meantime, the differences of the test ball revolution speed by these three types of electrodes are less than 1 %, which cross-validate the accuracy of the US-HCTEB.

The effects of the bearing lubrication state, environmental humidity, and bearing temperature on the output I_s of the US-HCTEB are illustrated in Fig. 4(e), (f), and (g), respectively. The considered bearing lubrication conditions were full-flood lubrication with oil flows of 15 L/min and 8 L/min and dry contact. The condition of full-flood lubrication is shown in **Video 1** (Supporting Information). Full-flood lubrication can be observed to significantly reduce the output I_s of the US-HCTEB with an amplitude below 2 nA. For rolling bearing in high-speed application scenarios, considering the influence of bearing skidding, oil-mixture lubrication is usually adopted. This method requires a very low amount of lubricant, which is closer to the scenario of dry contact than full flood lubrication. Therefore, it will not fundamentally change the working mechanism of US-HCTEB and the output can be guaranteed. Moreover, even under oil flood lubrication, it can still output stable

sinusoidal AC signal as an indicator for monitoring skidding. The influence of the environmental humidity on the US-HCTEB was evaluated using tests under different humidity values of 43%, 54%, 63%, and 80% with the temperature maintained between 20 and 25 °C, as shown in Fig. 4(f). It can be observed that the amplitude of I_s decreases from 33 to 17 nC with increasing humidity; thus, a dry environment favors the output of the US-HCTEB. Because the test platform did not include active heating facilities, the bearings were passively heated by long-term high-speed operation. Fig. 4(g) shows the I_s waveforms according to bearing outer ring temperatures of 30.7, 35.3, 40.7, 45.5, 50.1, and 54.8 °C. An increase in bearing temperature can be observed to slightly affect the US-HCTEB output; the amplitude of I_s changes by approximately 20% following a trend that first increases then decreases as the temperature increases within the test range.

Supplementary material related to this article can be found online at doi:10.1016/j.nanoen.2022.107759.

The skidding ratio b_{sk} of the US-HCTEB under the considered lubrication and environmental conditions is presented in Fig. 4(h). Owing to the drag effect of lubricating oil, the skidding ratio b_{sk} under full-flood lubrication is approximately six times higher than that under dry contact, reaching approximately 17%, which may damage the bearing raceway. Under high humidity, the overall b_{sk} increases significantly; the b_{sk} at 80% humidity is approximately three times that at 54%. The increase in bearing temperature can be observed to cause a slight increase in the overall b_{sk}, though the overall b_{sk} in this set of test conditions remains relatively low at less than 3%.

2.3. Superior performance of the US-HCTEB

To demonstrate the superiority of the proposed US-HCTEB, a durability test was conducted at 10,000 rpm for 50 h. To avoid premature failure of the bearing owing to a high temperature increase, the test platform was provided with forced air-cooling equipment, and the hydraulic loader only applied an axial preload. The bearing inner ring underwent a total of 30 million revolutions, 12.5 times those reported in a previous study [6], and the 0.2 s I_s waveform was recorded every 2 h. The bearing temperature increase over time is shown in Fig. 5(a), in which it can be observed that the increase in bearing temperature is insignificant under the applied forced-air cooling and light preload conditions. The output of the US-HCTEB remained stable during the entire long-term durability test. The SEM images of the rolling elements, raceways, and electrodes after the durability test are shown in Fig. S9 (Supporting Information). The rotational speed range of the US-HCTEB is compared with that of the triboelectric bearings reported in Refs. [6, 27,34,35,37–39,41,42] in Fig. 5(b). It can be observed that the maximum speed monitored by the US-HCTEB reaches 16000 rpm, which is more than three times that monitored by previously proposed sensors. Owing to the limitation of the maximum speed of the 6206 bearing itself (17000 rpm), the output was not evaluated at higher speeds. This illustrates the superiority of the US-HCTEB in monitoring the dynamic behavior of ultra-high-speed bearings.

To evaluate the effect of the TENG structure on the running performance of the US-HCTEB, the friction torque and vibration response of the US-HCTEB was compared to that of the original bearing without the TENG. The principle of the bearing friction torque test platform used to do so is illustrated in Fig. S10 and **Video 2** (Supporting Information). A comparison of the average friction torque and root mean square (RMS) values of the vibration acceleration of the US-HCTEB and original bearing at different ω_i values (300, 600, 900, 1200, and 1500 rpm) is presented in Fig. 5(c) and (d), respectively. The time-series of instantaneous friction torque is shown in Fig. S11 (Supporting Information). The values of these parameters for the original bearing and US-HCTEB can be observed to increase with increasing ω_i. At a low ω_i, the friction torque of US-HCTEB is approximately 30% higher than that of the original bearing; when ω_i is greater than 1200 rpm, the values are nearly equal. Because the US-HCTEB is primarily intended for use in high-speed
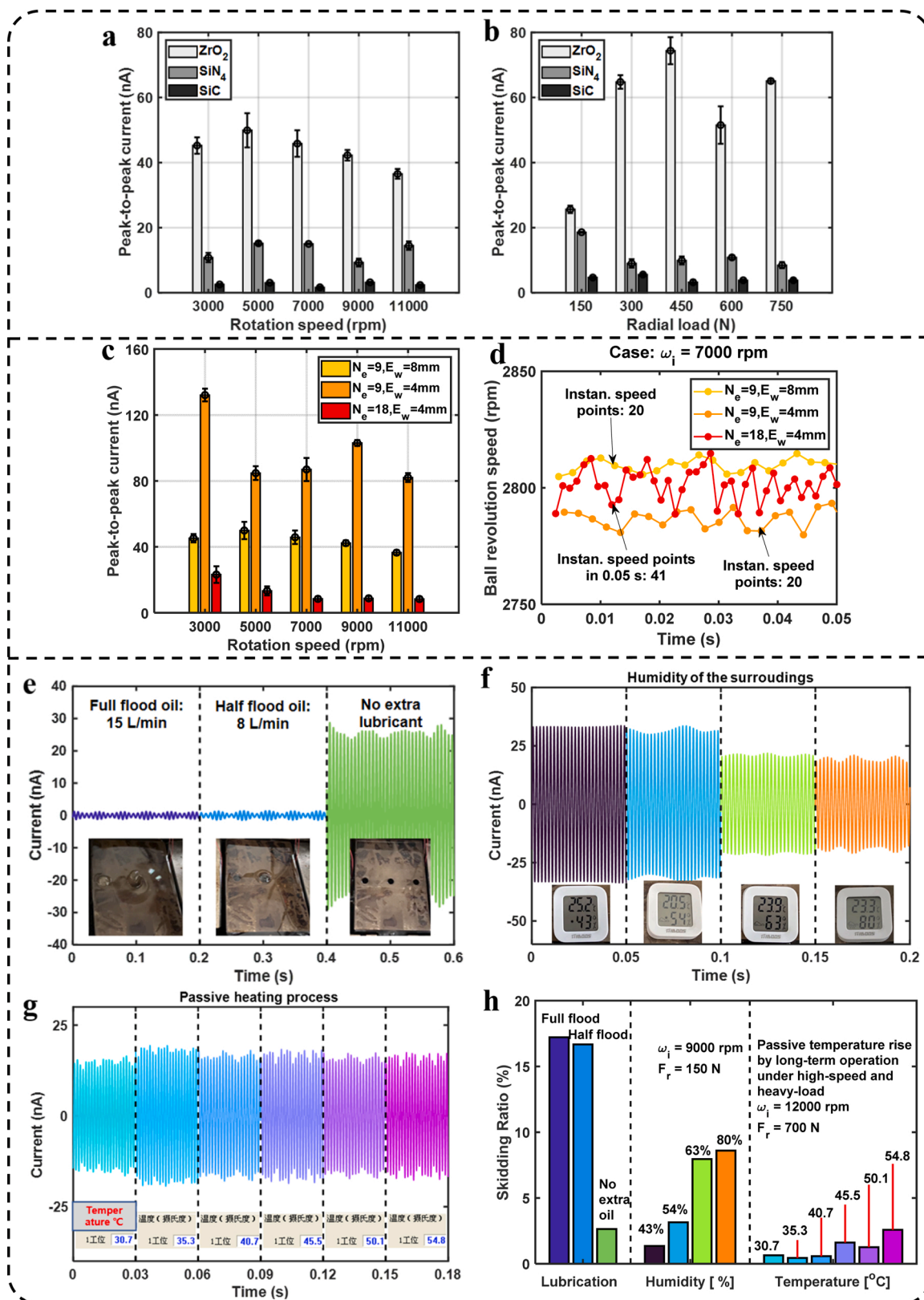
Fig. 4. Structural optimization and the effect of environmental conditions on US-HCTEB: the effect of different rolling element dielectric materials under (a) various speed, (b) various radial load; the effect of size and number of the electrode pair (c) on output current, (d) on sensor precision; the effect of (e) lubrication condition, (f) surrounding humidity, (g) bearing temperature on output performance; (h) the effect of lubrication, humidity, temperature on the overall skidding degree of US-HCTEB.
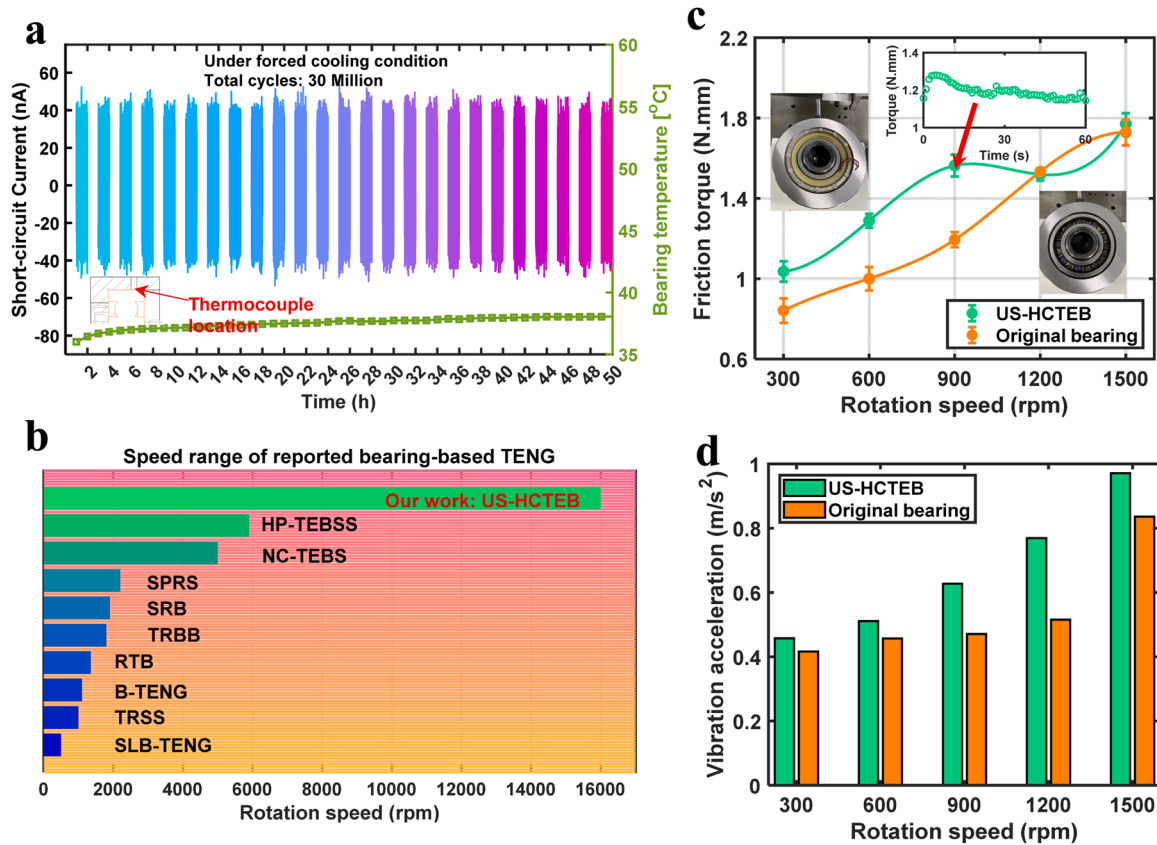
Fig. 5. The superior performance of US-HCTEB: (a) the output current of the US-HCTEB under durability test, with 30 million inner ring rotations, (b) comparison of the speed range of the US-HCTEB and the literature reported SLB-TENG [41], TRSS [38], B-TENG [42], RTB [27], TRBB [37], SRB [35], SPRS [34], NC-TEBS [39], HP-TEBSS [6] bearing-based TENGs, (c) comparison of the friction torque results of the US-HCTEB and the original rolling bearing, (d) comparison of the overall vibration acceleration level of the US-HCTEB and the original rolling bearing.

scenarios, it can be considered that the TENG has an insignificant effect on the bearing running state. From the perspective of vibration level, the US-HCTEB exhibited higher vibration than the original bearing. One possible reason for this is that the test was conducted on a friction torque test platform with a low support stiffness and therefore the vibrations could be an outcome of the fluctuations in the bearing mass center.

Supplementary material related to this article can be found online at doi:10.1016/j.nanoen.2022.107759.

3. Application of bearing dynamic instability monitoring

3.1. Skidding and stability performance

Rolling element skidding can lead to severe wear and smearing of the raceways and a rapid temperature increase in the bearing, thus reducing its operating stability and service life. The dynamic behavior monitoring capability of the US-HCTEB can be demonstrated by an analysis of bearing skidding and stability. The stability of the rolling element revolution speed also reflects the whirling and collision characteristics of the cage to a certain extent. Thus, it is critical to monitor these two parameters, especially in rolling bearings intended for use in high-speed equipment (e.g., turbochargers and turbofan engines). The output I_s of the US-HCTEB was therefore used to analyze the skidding and stability of the rolling elements in this study. A group of bearing skidding tests was conducted using a matrix of 54 combinations of working conditions, which can be found in Table S1(Supporting Information).

The overall b_{sk} can be calculated using fast Fourier transform (FFT), as shown in Fig. 3(e) and Eq. 4. The b_{sk} and RMS values of the rolling element I_s under the 54 considered operating conditions are shown in Fig. 6(a) and (b), respectively. The test time for each working condition

was 15 s. It can be observed that the variation of b_{sk} with increasing ω_i is notably different under different F_r values. Under a low value of F_r, $F_r =$ 50 N, the b_{sk} at a high rotational speed is slightly higher than that at medium and low rotational speeds. As F_r increases beyond 150 N, the b_{sk} of the US-HCTEB becomes significantly lower at higher speeds than that at lower speeds (although the absolute skidding velocity $f_{bm} - f_{br}$ at a high speed may be higher than that at a low speed) and approaches zero under most operating conditions at speeds higher than 10,000 rpm. A possible reason for this is that the rolling elements are inhibited from skidding under the dual action of the high contact load and centrifugal force at high rotational speeds. Notably, the b_{sk} of the US-HCTEB under radial load was found to be considerably smaller than that of an angular contact ball bearing under axial load [2,8]. Fig. 6(b) indicates that as F_r increases, the rotational speed corresponding to the maximum RMS value of I_s gradually decreases. When F_r is greater than 450 N, I_s exhibits a downward trend with increasing ω_i. A possible reason for this trend is the dual effect of the rapid increase in the bearing temperature under high speed and heavy load and the increased vibration of the bearing under high speed.

In addition to the overall skidding ratio of the rolling elements, the fluctuation range and distribution characteristics of the instantaneous revolution speed of the rolling elements are effective indicators for characterizing the running stability of the bearing. According to the working mechanism of the US-HCTEB, the instantaneous speed information pertaining to a rolling element can be obtained for every $1/Ne$ revolution. Fig. 6(c) shows the instantaneous speed fluctuation of a rolling element within 3 s and the overall revolution speed for the test case with $\omega_i = 15000$ rpm and $F_r = 750$ N; the range of speed fluctuation is approximately 2.15% of its overall value. The grouping shown in Fig. 6(d) is based on the deviation of the instantaneous speed from the
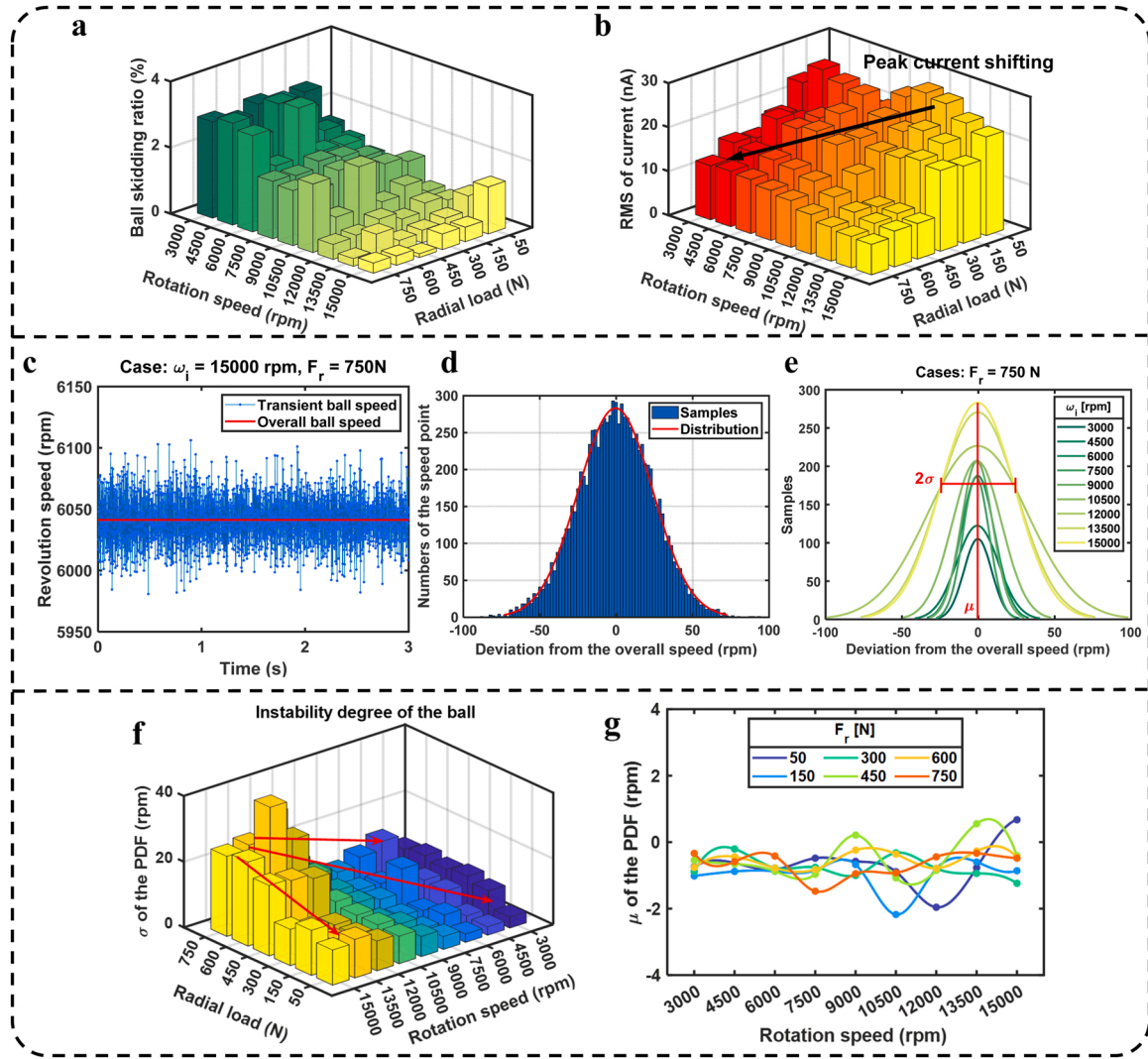
Fig. 6. The dynamic behavior of the rolling element monitored by US-HCTEB: (a) rolling element overall skidding ratio, and (b) the RMS of the output current of the US-HCTEB under various speed and radial load working conditions, (c) the instantaneous rolling element revolution speed of a selected example working condition, (d) Sample number distribution of the instantaneous speed point of the rolling element deviating from the overall speed, (e) the comparison of the sample distribution under different speed, (f) the σ, and (g) the μ of the PDF under various speed and radial load conditions, indicating the instability of bearing running state.

overall speed, with a range of 2 rpm for each group, and presents the frequency of the samples counted in each group for the 10 s instantaneous speed test (corresponding to the case depicted in Fig. 6(c)). The red line represents the optimal probability density function (PDF) curve obtained using the MATLAB distribution filter. The PDF estimation uses the normal distribution method, and its function is characterized by:

$$f(x) = \frac{1}{\sqrt{2\pi}\sigma} exp\left(-\frac{(x-\mu)^2}{2\sigma^2}\right) \tag{5}$$

where x is the speed deviation, μ and σ are the mean value and standard deviation of the speed distribution, respectively. From the perspective of the rolling element stability analysis, the smaller the σ, the more concentrated the instantaneous rotational speed distribution; and the closer μ is to zero, the more accurately the overall skidding ratio describes the instantaneous state of the rolling element; thus, the stability of the bearing can be considered to have improved. Examples of the σ, μ, and PDF curves under various ω_i values are shown in Fig. 6(e); they can be observed to present the characteristics of the rolling element revolution speed fluctuations in an intuitive and qualitative manner. The PDF curves and distributions for all test conditions are illustrated in Fig. S12 (Supporting Information). This is an innovative method for

evaluating bearing stability, it is difficult to obtain such precise information with traditional low-resolution eddy current testing method.

The results of the quantitative analysis of rolling element stability based on the above parameters are shown in Fig. 6(f) and (g), respectively, which present the σ and μ values for all test conditions. In the high-speed stage ($\omega_i > 10000$ rpm), the stability of the rolling elements decreases with increasing radial load because this load caused the rolling elements to frequently experience heavy load→ skidding→ light load cycles; this trend is less pronounced under a low ω_i. The fluctuation range of the absolute revolution speed at 15,000 rpm is approximately four times that at 3000 rpm. The μ value of the PDF is generally small, and its absolute value is within 2 rpm, indicating that the rolling element revolution speed obtained by the PDF estimation method was consistent with that obtained in the actual tests. This also indicates that the speed fluctuations were evenly distributed on both sides of the overall value.

3.2. Performance under extreme working conditions

The working conditions corresponding to various practical bearing application scenarios are typically complex and variable. Non-constant working conditions, such as rapid acceleration and deceleration, have

an overwhelming impact on the dynamic behavior and stability of the rolling components of bearings. Furthermore, such conditions may cause a bearing to fail early in its lifecycle. Bearing stability under variable working conditions is an extensive concerned and thorny issue in the industry, thus, its high precision real-time health monitoring is of great significance. Therefore, this study used the ultra-high-speed variable-frequency motorized spindle test platform to evaluate the dynamic behavior of the rolling elements and the output characteristics of the US-HCTEB under conditions of extremely rapid acceleration and deceleration.

The entire test for continuously variable conditions was divided into five phases: in the first phase, a constant speed of $\omega_i = 3000$ rpm was applied for 2 s; in the second phase, an extremely rapid acceleration of $\omega_i = 3000 \rightarrow 16000$ rpm was applied over 5.41 s with an acceleration rate of $a_i = 2400$ rpm/s; in the third phase, a constant speed of $\omega_i = 16000$ rpm was applied for 3.69 s; in the fourth phase, an extremely rapid deceleration of $\omega_i = 16000 \rightarrow 3000$ rpm was applied over 7 s with a deceleration rate of $a_i = -1857$ rpm/s; finally, the fifth stage was the
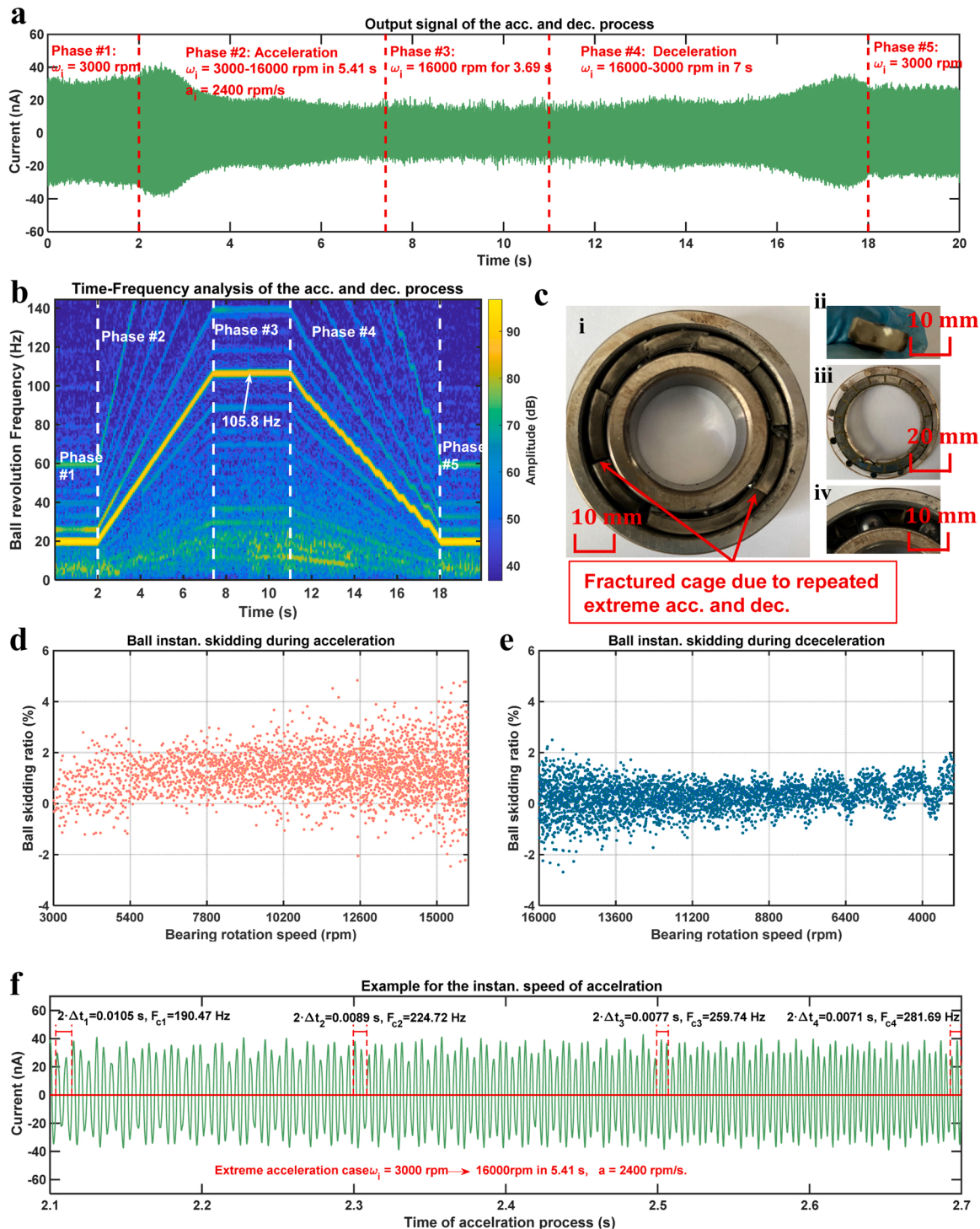

Fig. 7. The dynamic behavior of the US-HCTEB in extreme working condition: (a) the output current of the US-HCTEB under extremely fast acceleration and deceleration (b) the time-frequency spectrum analysis of the entire journey output current, (c) the failed bearing with fractured cage due to repeated extreme working condition, (d) the rolling element transient skidding ratio during acceleration and (e) deceleration, (f) magnified subplot (a) for indicating the acceleration process.

same as the first stage, with a constant speed of 3000 rpm for 2 s. The US-HCTEB output over the entire test is shown in Fig. 7(a). During both the acceleration and deceleration phases, the current amplitude waveform exhibits two "bulges," one large and one small; that is, two local extremes. This trend is consistent with the test results under a constant speed, as shown in Fig. 3 (a1).

A high sampling frequency of 102.4 kHz was used to acquire the output current signal during the test. Then, an FFT was performed on the acquired signal to obtain a high-resolution, three-dimensional time–frequency map over the entire test, as shown in Fig. 7(b). The ordinate corresponding to the dominant frequency in Fig. 7(b) is the real transient revolution frequency of the rolling element, as N_e has been divided. For example, in the third phase, the featured frequency of the US-HCTEB is 105.8 Hz, which is close to the 106.1 Hz featured frequency for the 6206 bearing cage; the difference between these values is deemed skidding. The dominant frequencies during acceleration and deceleration are also significant. Therefore, the US-HCTEB can effectively monitor extremely fast variable-speed conditions.

Because the overall b_{sk} of the bearing under radial load was small, it was difficult to quantify the skidding and stability characteristics during acceleration and deceleration in the time-frequency spectrum. Thus, the instantaneous b_{sk} of the rolling elements during the acceleration and deceleration phases are shown in Fig. 7(d) and (e), respectively. During the acceleration phase, the overall b_{sk} increases from 0.5% to 1.5% and the revolution speed fluctuation range increases from 3% to approximately 7% of ω_{bm} (the theoretical revolution speed of the rolling elements). Considering that ω_i increases by 5.3 times from 3000 rpm to 16000 rpm, the absolute speed fluctuation range increases by approximately 12 times. During the deceleration phase, because the bearing experienced a constant speed of 16000 rpm in the third phase, the speed fluctuation range is significantly smaller than that during the acceleration phase. Because the overall b_{sk} was suppressed during phase three, the overall b_{sk} is also lower during the deceleration phase. Considering that the applied deceleration was not perfectly linear but followed a stepped process, revolution speed fluctuation can also be observed in the corresponding characteristics. A magnified view of 0.6 s of the acceleration phase is provided in Fig. 7(f), in which it can be intuitively observed that the sinusoidal current waveform rapidly densifies; by calculating the period of this waveform, the instantaneous frequency of the rolling element can be determined to have rapidly increased. Fig. 7 (f) also illustrates the real-time performance of the US-HCTEB when monitoring the dynamic behavior of rolling elements.

This test resulted in an additional important finding. Under the multiple extreme long-term, heavy-load, and high-speed working conditions depicted in Fig. 7(a), the crown-shaped cage was subjected to the dual action of high temperature and high-speed centrifugal force. As the cage opening was turned outward in the radial direction of the bearing, it began to rub against the bearing outer ring, generating a high temperature that melted the PEEK and eventually led to sticking and fracture. Fig. 7(c) shows the bearing and its component structures after the bearing cage was fractured. Before this failure, the US-HCTEB was working normally, indicating that the designed TENG components are highly reliable and will not fail before the bearing. The SEM images of the electrodes, rolling elements, and melted cage after bearing failure corroborate this failure process and therefore prove the reliability of the TENG, as shown in Fig. S13 (Supporting Information). The detailed experimental dataset of the application of US-HCTEB can be found in Supporting Information.

4. Conclusion

A rolling element-based US-HCTEB with a crown-shaped cage was proposed to realize the real-time monitoring of bearing dynamic behavior and rolling element stability under ultra-high-speed and extremely variable-speed working conditions. The use of the floating, non-contact, rolling–sliding combination freestanding mode working principle ensured bearing structure integrity and bearing running independence. The output characteristics of the US-HCTEB were evaluated with various structural parameters and under various operating conditions. It was found that the output signal did not linearly increase by increasing the bearing radial load or rotation speed. The use of ZrO_2 rolling elements exhibited a more accurate output performance than the use of SiC or SiN_4 rolling elements. The overall skidding and rolling element instantaneous speed statistics suggest that the high speed of and heavy radial load on the US-HCTEB could reduce its overall skidding but increase its instability. Lubrication and environmental conditions were observed to have a significant influence on the output and skidding of the US-HCTEB and thus cannot be neglected. The US-HCTEB achieved output reliability and real-time performance at an ultra-high speed of 16000 rpm and a high DN value of 0.48×10^6 mm·rpm, which far exceeds the limits of previously reported triboelectric bearings. A durability test applying 30 million speed cycles to the US-HCTEB also demonstrated its superiority among triboelectric bearings. The application of the US-HCTEB in extremely variable working conditions showed that the proposed intelligent bearing exhibits wide applicability and high-resolution dynamic behavior identification. The most surprising finding was that the TENG assembly provided exceptionally high reliability and did not fail before the bearing. Thus, the proposed high-precision US-HCTEB represents an essential basis for the development of intelligent bearings.

5. Experimental methods

5.1. Fabrication of the US-HCTEB prototype

Epoxy resin plates covered with different types of electrodes were manufactured by the Jiawen Electronic Company. The 6206 hybrid ceramic rolling bearings employed in this study were custom-made by NSK Ltd. A PCB with backing glue (MT-101) was adhered to the acrylic end cover. Twelve strong neodymium-boron magnets, custom-made by Haomei Company, were embedded on the acrylic end cover. All components were prepared and assembled as shown in Fig. 1(a) and (c) to complete the fabrication of the US-HCTEB prototype.

5.2. Designing the high-speed bearing test platform

The test platform for the US-HCTEB tests conducted in this study was an ABLT-A bearing life enhancement testing machine developed by the Hangzhou Bearing Test & Research Center. It consisted of a high-speed electric spindle (3000–30000 rpm), driving shaft (diameter range 20–80 mm), frequency converter (SKI600–1D5G-4), and hydraulic loading system to apply radial and axial loads to the bearing.

5.3. Output signal measurement and postprocessing

The short circuit current, open circuit voltage and transferred charge of the US-HCTEB are measured using a Keithley 6514 electrostatic meter. The acceleration signal is measured by accelerometer (PCB 352C04). Both the output voltages are determined by an analog-to-digital converter (Econ MI-7004, 4-channel voltage measurement module, Econ Technologies Co. Ltd.). The electric signal which measured by electrostatic meter and voltage signal of the accelerometer are acquired by ECON DAS 4.2.36, and the data postprocessing are implemented by MATLAB 2021a.

CRediT authorship contribution statement

S. Gao: Conceptualization, Data curation, Formal analysis, Investigation, Methodology, Software, Visualization, Writing – original draft, Writing – review & editing. **Q. Han:** Conceptualization, Formal analysis, Funding acquisition, Investigation, Project administration, Resources, Validation, Writing – review & editing. **X. Zhang:** Investigation,

Methodology, Resources. **P. Pennacchi:** Funding acquisition, Resources, Supervision, Validation, Writing – review & editing. **F. Chu:** Project administration, Resources, Supervision.

Declaration of Competing Interest

The authors declare that they have no known competing financial interests or personal relationships that could have appeared to influence the work reported in this paper.

Data Availability

Data will be made available on request.

Appendix A. Supporting information

Supplementary data associated with this article can be found in the online version at doi:10.1016/j.nanoen.2022.107759.

References

[1] Y. Qin, C. Li, X. Wu, Y. Wang, H. Chen, Multiple-degree-of-freedom dynamic model of rolling bearing with a localized surface defect, Mech. Mach. Theory 154 (2020), 104047.

[2] S. Gao, S. Chatterton, L. Naldi, P. Pennacchi, Ball bearing skidding and over-skidding in large-scale angular contact ball bearings: Nonlinear dynamic model with thermal effects and experimental results, Mech. Syst. Signal Process. 147 (2021), 107120.

[3] S. Gao, Q. Han, N. Zhou, P. Pennacchi, F. Chu, Stability and skidding behavior of spacecraft porous oil-containing polyimide cages based on high-speed photography technology, Tribol. Int. 165 (2022), 107294.

[4] S. Gao, Q. Han, N. Zhou, P. Pennacchi, S. Chatterton, T. Qing, J. Zhang, F. Chu, Experimental and theoretical approaches for determining cage motion dynamic characteristics of angular contact ball bearings considering whirling and overall skidding behaviors, Mech. Syst. Signal Process. 168 (2022), 108704.

[5] L. Cui, J. Huang, F. Zhang, F. Chu, Activation of CXCL5-CXCR2 axis promotes proliferation and accelerates G1 to S phase transition of papillary thyroid carcinoma cells and activates JNK and p38 pathways, Mech. Syst. Signal Process. 120 (2019) 608–616.

[6] S. Gao, Q. Han, Z. Jiang, X. Zhang, P. Pennacchi, F. Chu, Triboelectric based high-precision self-powering cage skidding sensor and application on main bearing of jet engine, Nano Energy 99 (2022) 107387.

[7] W. Kwak, J. Lee, Y.B. Lee, Theoretical and experimental approach to ball bearing frictional characteristics compared with cryogenic friction model and dry friction model, Mech. Syst. Signal Process. 124 (2019) 424–438.

[8] Q. Han, F. Chu, Stabilisation of microalgae: Iodine mobilisation under aerobic and anaerobic conditions, J. Sound Vib. 354 (2015) 219–226.

[9] S. Gao, Q. Han, N. Zhou, F. Zhang, Z. Yang, S. Chatterton, P. Pennacchi, Nonlinear Dyn. (2022) 3.

[10] S. Gao, S. Chatterton, P. Pennacchi, F. Chu, Behaviour of an angular contact ball bearing with three-dimensional cubic-like defect: a comprehensive non-linear dynamic model for predicting vibration response, Mech. Mach. Theory 163 (2021), 104376.

[11] Y. Cui, S. Deng, R. Niu, G. Chen, Vibration effect analysis of roller dynamic unbalance on the cage of high-speed cylindrical roller bearing, J. Sound Vib. 434 (2018) 314–335.

[12] S. Gao, Q. Han, P. Pennacchi, S. Chatterton, F. Chu, Friction (2022), https://doi.org/10.1007/s40544-022-0622-9.

[13] D. Hu, W. Wang, X. Zhang, K. Chen, On-line real-time mistuning identification and model calibration method for rotating blisks based on blade tip timing (BTT, Mech. Syst. Signal Process. 147 (2021), 107074.

[14] B. Choe, W. Kwak, D. Jeon, Y. Lee, Experimental study on dynamic behavior of ball bearing cage in cryogenic environments, Part II: effects of cage mass imbalance, Mech. Syst. Signal Process. 116 (2019) 25–39.

[15] Z. Yang, X. Niu, C. Li, IEEE Trans. Instrum. Meas. 9456 (2022), 3171605.

[16] Z.L. Wang, Triboelectric nanogenerators as new energy technology and self-powered sensors – principles, problems and perspectives, Faraday Discuss. 176 (2014) 447–458.

[17] F.R. Fan, Z.Q. Tian, Z.Lin Wang, Flexible triboelectric generator, Nano Energy 1 (2012) 328–334.

[18] S. Wang, Y. Xie, S. Niu, L. Lin, Z.L. Wang, Freestanding triboelectric-layer-based nanogenerators for harvesting energy from a moving object or human motion in contact and non-contact modes, Adv. Mater. 26 (2014) 2818–2824.

[19] J. Chung, D. Heo, G. Shin, D. Choi, K. Choi, D. Kim, S. Lee, Adv. Energy Mater. 9 (2019) 1.

[20] J. Han, Y. Feng, P. Chen, X. Liang, H. Pang, T. Jiang, Z.L. Wang, Tunable Bi-directional photoresponse in hybrid PtSe2−xThin films based on precisely controllable selenization engineering, Adv. Funct. Mater. 32 (2022) 1.

[21] H. Wu, J. Wang, Z. Wu, S. Kang, X. Wei, H. Wang, H. Luo, L. Yang, R. Liao, Z. L. Wang, Eight-electron redox cyclohexanehexone anode for high-rate high-capacity lithium storage, Adv. Energy Mater. 12 (2022) 1.

[22] Y. Xie, S. Wang, S. Niu, L. Lin, Q. Jing, J. Yang, Z. Wu, Z.L. Wang, Grating-structured freestanding triboelectric-layer nanogenerator for harvesting mechanical energy at 85 % total conversion efficiency, Adv. Mater. 26 (2014) 6599–6607.

[23] Q. Jing, Y. Xie, G. Zhu, R.P.S. Han, Z.L. Wang, Association between insulin-like growth factor-1 and cardiovascular disease risk: Evidence from a meta-analysis, Nat. Commun. 6 (2015) 1–5.

[24] C. Shan, W. He, H. Wu, S. Fu, Q. Tang, Z. Wang, Y. Du, J. Wang, H. Guo, C. Hu, Adv. Energy Mater. 2200963 (2022) 1.

[25] L. Long, W. Liu, Z. Wang, W. He, G. Li, Q. Tang, H. Guo, X. Pu, Y. Liu, C. Hu, Nat. Commun. 12 (2021) 1.

[26] H. Lin, Y. Liu, S. Chen, Q. Xu, S. Wang, T. Hu, P. Pan, Y. Wang, Y. Zhang, N. Li, Y. Li, Y. Ma, Y. Xie, L. Wang, Seesaw structured triboelectric nanogenerator with enhanced output performance and its applications in self-powered motion sensing, Nano Energy 65 (2019), 103944.

[27] Z. Jiang, S. Gao, Y. Kong, P. Pennacchi, F. Chu, Q. Han, Ultra-compact triboelectric bearing based on a ribbon cage with applications for fault diagnosis of rotating machinery, Nano Energy 99 (2022), 107263.

[28] Z. Yuan, G. Shen, C. Pan, Z.L. Wang, Flexible sliding sensor for simultaneous monitoring deformation and displacement on a robotic hand/arm, Nano Energy 73 (2020), 104764.

[29] J. Chen, Z.L. Wang, Reviving vibration energy harvesting and self-powered sensing by a triboelectric nanogenerator, Joule 1 (2017) 480–521.

[30] Z. Zhao, X. Pu, C. Du, L. Li, C. Jiang, W. Hu, Z.L. Wang, Freestanding flag-type triboelectric nanogenerator for harvesting high-altitude wind energy from arbitrary directions, ACS Nano 10 (2016) 1780–1787.

[31] H. Guo, J. Chen, L. Wang, A.C. Wang, Y. Li, C. An, J.-H. He, C. Hu, V.K.S. Hsiao, Z. L. Wang, A highly efficient triboelectric negative air ion generator, Nat. Sustain. 4 (2021) 147–153.

[32] K. Dong, X. Peng, Z.L. Wang, Fiber/fabric-based piezoelectric and triboelectric nanogenerators for flexible/stretchable and wearable electronics and artificial intelligence, Adv. Mater. 32 (2020), 1902549.

[33] Q. Gao, T. Cheng, Z.L. Wang, Triboelectric mechanical sensors—Progress and prospects, Extrem. Mech. Lett. 42 (2021), 101100.

[34] X.S. Meng, H.Y. Li, G. Zhu, Z.L. Wang, Screening of HIV-1 protease using a combination of an ultra-high-throughput fluorescent-based assay and rapidfire mass spectrometry, Nano Energy 12 (2015) 606–615.

[35] D. Choi, T. Sung, J.Y. Kwon, Rotation sensing systems: a self-powered smart roller-bearing based on a triboelectric nanogenerator for measurement of rotation movement, Adv. Mater. Technol. 3 (2018) 1.

[36] J. Yang, Y. Sun, J. Zhang, B. Chen, Z.L. Wang, Biting pain reproduced by the tooth slooth: aid for early diagnosis of cracked tooth, Cell Rep. Phys. Sci. 2 (2021) 0.

[37] Q. Han, Z. Ding, Z. Qin, T. Wang, X. Xu, F. Chu, A triboelectric rolling ball bearing with self-powering and self-sensing capabilities, Nano Energy 67 (2020), 104277.

[38] Z. Xie, J. Dong, Y. Li, L. Gu, B. Song, T. Cheng, Z.L. Wang, Triboelectric rotational speed sensor integrated into a bearing: A solid step to industrial application, Extrem. Mech. Lett. 34 (2020), 100595.

[39] Z. Xie, Y. Wang, R. Wu, J. Yin, D. Yu, J. Liu, T. Cheng, A high-speed and long-life triboelectric sensor with charge supplement for monitoring the speed and skidding of rolling bearing, Nano Energy 92 (2022), 106747.

[40] H. Yang, W. Liu, Y. Xi, M. Lai, H. Guo, G. Liu, M. Wang, T. Li, X. Ji, X. Li, Rolling friction contact-separation mode hybrid triboelectric nanogenerator for mechanical energy harvesting and self-powered multifunctional sensors, Nano Energy 47 (2018) 539–546.

[41] M. Song, J. Chung, S.H. Chung, K. Cha, D. Heo, S. Kim, P.T.J. Hwang, D. Kim, B. Koo, J. Hong, S. Lee, Semisolid-lubricant-based ball-bearing triboelectric nanogenerator for current amplification, enhanced mechanical lifespan, and thermal stabilization, Nano Energy 93 (2022), 106816.

[42] X.H. Li, C.B. Han, T. Jiang, C. Zhang, Z.L. Wang, A ball-bearing structured triboelectric nanogenerator for nondestructive damage and rotating speed measurement, Nanotechnology 27 (2016) 85401.

Shuai Gao received the B.S. and M.S. degree in mechanical engineering from Beijing university of Chemical Engineering, Beijing, China in 2015 and 2018. He was a visiting scholar in the Department of Mechanical Engineering at Tsinghua University, Beijing, China. He is currently a Ph. D. candidate in Department of Mechanical Engineering at Politecnico di Milano, Italy. His research interests focus on the rotor dynamics, triboelectric nanogenerators, and bearing fault diagnostics.

Prof. Paolo Pennacchi is currently a full professor in Department of Mechanical Engineering at Politecnico di Milano, Italy. He received his Ph. D degree in Mechanical Engineering from Politecnico di Milano in 1997. He was the Chair of the 9th IFToMM International Conference on Rotor Dynamics, 2014. His main research interests focus on rotor dynamics, and diagnostics and identification of rotating machines.

Dr. Qinkai Han is currently an associate professor in Department of Mechanical Engineering at Tsinghua University. He received his Bachelor degree in Aircraft Engineering (2004) and Ph.D. degree from College of Energy and Power Engineering (2010) at BeiHang University. His interests focus on the development of self-powered system, wind energy harvesting, and application based on triboelectric nanogenerator.

Prof. Fulei Chu is currently a professor in Department of Mechanical Engineering at Tsinghua University. He received his Ph.D. degree in Mechanical Engineering from Southampton University in 1993. He was awarded the National Science Fund for Distinguished Young Scholars in 2004. His research interests focus on nanogenerators, self-powered systems, and energy harvesting technology.

Dr. Xuening Zhang received the Ph. D. degree in mechanical engineering from Tsinghua University, Beijing, China, in 2014. He is currently a senior engineer specialized in the fields of rotordynamics for high speed rotating structures at Aero Engine Academy of China. His research interests include active vibration control of flexible shafts and dynamics of rolling element bearings.